AGU PUBLICATIONS

JGR

Journal of Geophysical Research: Planets

RESEARCH ARTICLE

10.1002/2016JE005090

Key Points:

- Complex craters in the three different lunar terranes have differing gravity signals
- Differences in crater gravity signals between the lunar terrane are best explained by porosity variations
- Global Modeling only explains 10% of crater variance. Detailed modeling will be needed to better understand individual crater signals

Supporting Information:

- Supporting Information S1
- Table S1

Correspondence to:
C. J. Bierson,
cthomas1@ucsc.edu

Citation:
Bierson, C. J., R. J. Phillips, F. Nimmo, J. Besserer, C. Milbury, J. T. Keane, J. M. Soderblom, and M. T. Zuber (2016), Interactions between complex craters and the lunar crust: Analysis using GRAIL data, *J. Geophys. Res. Planets*, *121*, 1488–1497, doi:10.1002/2016JE005090.

Received 31 MAY 2016
Accepted 8 AUG 2016
Accepted article online 11 AUG 2016
Published online 25 AUG 2016

Interactions between complex craters and the lunar crust: Analysis using GRAIL data

C. J. Bierson[1], Roger J. Phillips[2,3], Francis Nimmo[1], Jonathan Besserer[4], Colleen Milbury[5], James T. Keane[6], Jason M. Soderblom[7], and Maria T. Zuber[7]

[1]Department of Earth and Planetary Sciences, University of California, Santa Cruz, California, USA, [2]Planetary Science Directorate, Southwest Research Institute, Boulder, Colorado, USA, [3]McDonnell Center for the Space Sciences and Department of Earth and Planetary Sciences, Washington University, St. Louis, Missouri, USA, [4]Enseignant Indépendant (SIREN 819716788), Nantes, France, [5]Department of Earth, Atmospheric, and Planetary Sciences, Purdue University, West Lafayette, Indiana, USA, [6]Lunar and Planetary Laboratory, University of Arizona, Tucson, Arizona, USA, [7]Department of Earth, Atmospheric and Planetary Sciences, Massachusetts Institute of Technology, Cambridge, Massachusetts, USA

Abstract A high-resolution gravity map over the entire lunar surface has been derived from data acquired by the Gravity Recovery and Interior Laboratory (GRAIL) mission. Soderblom et al. (2015) showed that crater Bouguer gravity anomalies scale with crater diameter and porosity for craters in the lunar highlands. Here we extend this study globally, examining complex craters in each of the three lunar terranes: highlands, maria, and the South Pole-Aitken basin. We find that craters within South Pole-Aitken basin and in the lunar maria have statistically different Bouguer anomalies from those in the lunar highlands. These differences are best explained by differences in crustal porosity among the three terranes. Though there is still much unresolved scatter in the data, we find that no other lunar material properties (crustal thickness, density gradient, etc.) are able to improve our model fit to the data.

1. Introduction

One of the primary objectives of the Gravity Recovery and Interior Laboratory (GRAIL) mission [*Zuber et al.*, 2013a] was to use the Bouguer gravity anomaly (g_B) of craters to learn about both the subsurface disposition beneath craters (e.g., extent of brecciation) and as a tool to understand the structure of the lunar crust. Such investigations date back to the post-Apollo decade but were limited by resolution and coverage [*Dvorak and Phillips*, 1977; *Sugano and Heki*, 2004]. The GRAIL mission has provided a lunar gravity field of unprecedented resolution, allowing long-standing questions regarding the effects of impacts on the lunar crust to be quantitatively addressed.

The Bouguer gravity is the observed free-air gravity, represented by a spherical harmonic model, with the effect of topography removed assuming a constant crustal density [*Zuber et al.*, 2013b]. Topographic information is provided by the Lunar Orbiter Laser Altimeter (LOLA) [*Smith et al.*, 2010]. The GRAIL Bouguer gravity used in this study resolves craters larger than ∼12 km in diameter. In addition, GRAIL resolves the rich and varied background of geological signals both within and surrounding the vast majority of complex craters. The result is that the crater signal can be obscured and is often not conducive to geophysical modeling. One way to deal with this problem is to examine craters not on an individual basis but to look for statistically meaningful trends within an ensemble of craters. This requires using a single characterizing metric, $\bar{g}_B$, often the mean value of the Bouguer anomaly out to some radial distance (section 1.2). Even so, there is a long-wavelength (regional) g_B background signal that must be removed for each crater. If done improperly, this can result in fictitious trends between $\bar{g}_B$ and other parameters (e.g., $\bar{g}_B$ versus diameter) or scatter in an ensemble of Bouguer anomalies.

1.1. Sources of Crater Bouguer Anomalies

The crater Bouguer anomaly, $\bar{g}_B$, is proportional to the density contrast, $\Delta\rho$, between material beneath the crater and the surrounding country rock. Assuming for illustrative purposes, a constant grain density, ρ_g, we can relate $\bar{g}_B$ to the porosity, ϕ, contrast by noting (i = beneath the crater; o = outside the crater):

$$\bar{g}_B \propto \Delta\rho = (\phi_o - \phi_i)\rho_g. \tag{1}$$

This equation shows that Bouguer gravity measurements are a proxy for porosity variations induced by the cratering process. Craters that formed in low-porosity regions fracture and shear the preexisting material forming a higher-porosity zone and thereby a negative Bouguer signal [*Milbury et al.*, 2015]. In regions where the crust is already highly porous, fracturing can only play a limited role in creating new porosity; rather, the passage of the shockwave through the material compresses it forming a higher-density zone and thereby a positive $\bar{g_B}$. Other effects, like structural uplift and magmatic intrusions, can also create positive $\bar{g_B}$s. In principle, craters with negative $\bar{g_B}$ in the same region but with different diameters will yield information on the depth dependence of the crustal porosity detected by GRAIL [*Wieczorek et al.*, 2013; *Besserer et al.*, 2014]. It should be noted that ρ_g is not constant over the surface of the Moon and can be altered by the high shock pressures during impacts [*Stoffler et al.*, 1975]. Relative to the bulk density, ρ_g as inferred from spectroscopy shows little variation over the surface of the Moon [*Huang and Wieczorek*, 2012]. This is discussed further in section 5.

For this work it is important to understand the GRAIL-derived crustal density models. *Wieczorek et al.* [2013] estimated the bulk density, ρ_b, of the top few kilometers of the crust, and later, *Besserer et al.* [2014] used the wavelength dependence of potential field attenuation to estimate the vertical density profile by assuming either a linear or an exponential depth dependence. Only the linear model provides an estimate of the density structure of the lunar maria regions, though such results should be used cautiously. In the maria, basalts of high grain density and low porosity (less fractured) overlie low grain density and high porosity (highly fractured) anorthositic crust. The density structure at SPA is less well understood but may involve a dense impact melt sheet and an impact-induced annealing of fractures [*Vaughan and Head*, 2014]. The SPA region exhibits a unique combination of low-porosity, high bulk density, and low *e*-folding depth [*Besserer et al.*, 2014].

These density estimates can be used to calculate the porosity of the lunar crust via

$$\phi = 1 - \frac{\rho_b}{\rho_g}. \tag{2}$$

Estimates of the grain density of the lunar crust are obtained from spectroscopic observations [*Huang and Wieczorek*, 2012] and empirical data [*Kiefer et al.*, 2012]. Spectroscopic observations are, however, only sensitive to the upper few centimeters of the lunar regolith. To apply equation (2) to the lunar crust, it is assumed that this ρ_g is constant with depth. This assumption is reasonable for the lunar highlands upper crust where there is no evidence for any compositional changes with depth [*Jolliff et al.*, 2000; *Wieczorek et al.*, 2006]. The lunar maria and SPA, however, have a more complex vertical structure as described above. For each crater, the point estimate of density was done by interpolation of the density grid provided by *Wieczorek et al.* [2013] or *Besserer et al.* [2014]. Grain density estimates were done by expanding the spherical harmonic solution of *Huang and Wieczorek* [2012] to degree and order 310. Using either density or grain density estimates from the area surrounding the crater as oppose to within the crater has no notable effect due to the low resolution of these data sets.

1.2. Measures of Crater $\bar{g_B}$

There are a multitude of ways to define $\bar{g_B}$ for a given crater. Each crater has radial and azimuthal variations in g_B. Because of this, any value given to describe a crater's g_B will be an oversimplification. The goal of any single measure of g_B is to, in aggregate, give some insight into the the primary processes responsible for the formation of crater g_B signals.

For this work, we assume that the signal associated with a given crater is radially symmetric. To measure this signal, each crater is divided into annuli of width $D/40$, where D is the crater diameter. This creates a radially averaged profile for each crater. *Pilkington and Grieve* [1992] defined the minimum of the radial profile of each crater as the g_B signal. *Soderblom et al.* [2015] define two g_B measures. The central Bouguer anomaly is defined as the area-weighted mean within 0.2 radii of the center and the residual Bouguer anomaly as the area-weighted mean out to the full crater radius. Each of these subtract off a mean background value to remove regional signals.

Measures of the g_B near the center of the crater are more sensitive to mantle uplift signals for craters larger than ~140 km in diameter [*Milbury et al.*, 2015]. This is also true when using the maximum azimuthally averaged g_B because the radial profile often peaks in the crater center. Using the minimal radial g_B emphasizes the component due to fracturing. For this work we use the full radius mean, $\bar{g_B}$, to try and capture the multitude of effects present. This measure differs from the residual Bouguer anomaly of *Soderblom et al.* [2015] in that we use a filter in the spherical harmonic domain to remove regional signals instead of subtracting a constant value (see section 2.1).

1.3. Overview

In this paper, we discuss the steps that we took to obtain clear estimates of crater Bouguer anomalies. We examine the global statistics of $\bar{g_B}$ versus D and ϕ. These relationships were noted by *Soderblom et al.* [2015] and *Milbury et al.* [2015]. We expand on this previous work by examining the interactions between these parameters. Furthermore, we show that the significant scatter about the linear trends are largely due to stochastic behavior of g_B at different length scales but that the linear trends are robust. We also examine and interpret spatial correlations of $\bar{g_B}$ to ϕ, and bulk density. In particular, we contrast the three major lunar terranes: South Pole-Aitken Basin, farside highlands, and the maria [*Jolliff et al.*, 2000].

2. Data Set

We estimated $\bar{g_B}$ for about 4000 craters. We used the JPL 900C11A gravity model [*Konopliv et al.*, 2014].The Bouguer anomaly was calculated by subtracting from each free-air gravity coefficient the corresponding coefficient of the gravity contribution of finite amplitude topography using a constant density of 2560 kg m^{-3} [*Wieczorek et al.*, 2013]. The resolution of the Bouguer gravity model corresponds to spherical harmonic degree $l = 600$, corresponding to a spatial resolution of ∼20 km. We did not include any craters with a diameter of less than 30 km. An upper diameter limit was set at 200 km in order to exclude the effects of mantle uplift [*Milbury et al.*, 2015; *Soderblom et al.*, 2015] and/or flexure. For calculating g_B, the spherical harmonic coefficients were expanded into a simple cylindrical map projection. A limited number of craters were used at latitudes greater than 60°, and the solutions were expanded in a polar stereographic projection to prevent any bias in taking radial means around the crater center.

For each crater, a minimum degree of expansion, $l_{\min}$, could be set dynamically to any value from 1 to 130 (discussed more in the following section). All data were expanded to a maximum degree and order of 600. A 20° cosine taper to prevent ringing was applied to both the high and low end of the spectrum. For this work we define $\bar{g_B}$ as the mean of the g_B within the crater rim as defined by *Head et al.* [2010] (see section 1.2).

2.1. Background Removal

One of the difficulties in understanding the Bouguer anomaly associated with relatively small features is that it is often overwhelmed by larger, long-wavelength regional signals. Past work has tried to get around this by subtracting the mean Bouguer anomaly in a background annulus from the crater signal [*Sugano and Heki*, 2004; *Soderblom et al.*, 2015]. In order to better resolve spatially the Bouguer signal of individual craters, we implement an alternative technique. We apply a high-pass filter in the spherical harmonic domain that scales with the crater diameter. This was done with

$$l_{\min} = \frac{2\pi R_0}{n \cdot D}, \tag{3}$$

where R_0 is the radius of the Moon and n is a nondimensional scaling factor. It should be noted that, due to the wavelength dependence of attenuation, some bias may be introduced by equation (3) if the depth of the crater g_B does not scale with crater Diameter.

It can be shown that annulus removal and high-pass filtering are statistically equivalent processes. Defining an annulus with outer and inner radii of $kD/2$ and $kD/2 - D/4$, respectively, a scatter plot comparing these approaches has a slope of unity when $k = n/2$ (outer radius $= D$) (Figure 1a). The annulus is a localizing window in the spatial domain, whose spectrum is convolved with the spectrum of g_B. When $n = 4$, the cutoff harmonic $l_{\min}$ follows very closely the first spectral peak of the annulus spectrum as D varies (Figure 1b), providing an explanation for the equivalence of the two approaches.

While statistically equivalent, these approaches are not identical. The long-wavelength filtering removes not only the value but also the shape of the background signal. To illustrate this, two example craters are shown in Figure 2. In both cases the crater signals are swamped by a long-wavelength background signal. Changing $l_{\min}$ removes this background signal revealing signals that are well correlated with the crater itself. In our comparisons we have not found any craters that have a better resolved anomaly with the background removal technique.

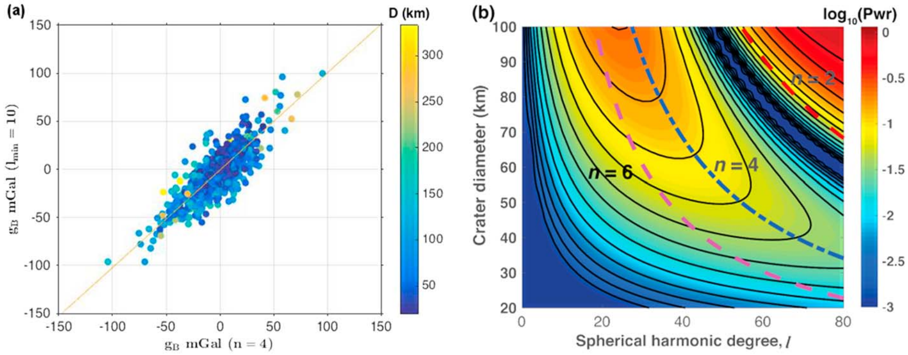

Figure 1. Comparison of Bouguer anomaly for each crater (a) calculated using spectral filtering (equation (3)) with $n = 4$ (x axis) with a constant cutoff of $l_{\mathrm{min}} = 10$, with background removal of mean value in an annulus defined by $kD/2$ and $kD/2 - D/4$ (y axis). The background annulus was defined using $k = 2$ for each crater. A least squares linear fit gives a slope of 1.01. (b) Spectral power in an annulus $0.75D$ to D ($k = 2$). Also plotted are D versus l_{min} curves for three values of n. The $n = 4$ curve follows the first spectral peak, and this is repeatable for different pairs of annulus radii and n based on $k = n/2$.

The Bouguer anomaly of any feature of finite size will have some amount of power at all spherical harmonic degrees. We estimate the amount of crater signal power lost by this filtering by calculating the root-mean-square (RMS) power spectrum of a uniform density spherical cap. For craters in our diameter range, a filter with $n = 3$ loses $\sim$ 60% of the crater power; $n = 4$ is 50%, and $n = 5$ is $\sim$ 40%. We elect to use $n = 4$ because it effectively removes the background signal without losing too much power from the crater itself.

2.2. Filtering Out Noisy Craters

We would expect that if a crater existed in isolation, it would have a roughly axisymmetric g_B signal. For estimating noise at scales of order D, we use a measure of the standard deviation within the crater, σ_{in}, that characterizes the departure of g_B from axisymmetry. In order to limit the contribution of radial signals to this measure, we define σ_{in} as the area-weighted mean of the standard deviation within each annulus within the crater. Craters with a high σ_{in} show an anomaly not associated with the crater or an anomaly that is not symmetric. We rejected craters with $\sigma_{\mathrm{in}} > 30$ mGal, with this cutoff value chosen empirically.

We also calculated a standard deviation, σ_{out}, for g_B bounded by annuli of $0.5D$ and $0.75D$, which is similar to a measure used by *Soderblom et al.* [2015] to reject noisy craters. We found that σ_{out} can be large due to surrounding craters or other features not associated with the crater itself. Still, there is a significant decrease in the data variance as the cutoff value of σ_{out} is decreased. Simply stated, the subtraction of an annulus mean to obtain $\bar{g}_B$ is compromised by a large value of the corresponding standard deviation, which represents an estimate of the uncertainty in the mean background level. Using a dynamic high-pass filter does not eliminate this problem. However, parametric estimates, such as the slope of $\bar{g}_B$ versus D in a crater collection are insensitive to the cutoff value, implying that this noise has zero mean over the crater set and that parametric estimates are unbiased despite the presence of substantial scatter.

2.3. Monte Carlo Runs and Mass Deficit Plots

To ensure that our results were not due to the characteristics of the lunar crust alone or to an artifact of our data processing, Monte Carlo simulations were carried out for locations with random latitudes, longitudes, and crater diameters. Five sets, each of 250 synthetic craters, were generated. The latitude and longitude were randomly generated such that any unit area had the same probability of being picked. Diameter values were randomly drawn from values in the real crater database to make sure that the distribution of diameter values was the same as that of the real craters. The resulting "craters" were processed by the exact same procedure employed for the real craters in our database. For linear correlations like those discussed in *Soderblom et al.* [2015] and those presented below (e.g., g_B versus D) no trends were found in the Monte Carlo "craters." There was, however, a spurious trend for power fits to the crater mass deficit, as described below.

In the crater gravity literature [*Dvorak and Phillips*, 1977; *Pilkington and Grieve*, 1992] it is common to look for a relationship that follows

$$\Delta M = CD^m. \tag{4}$$

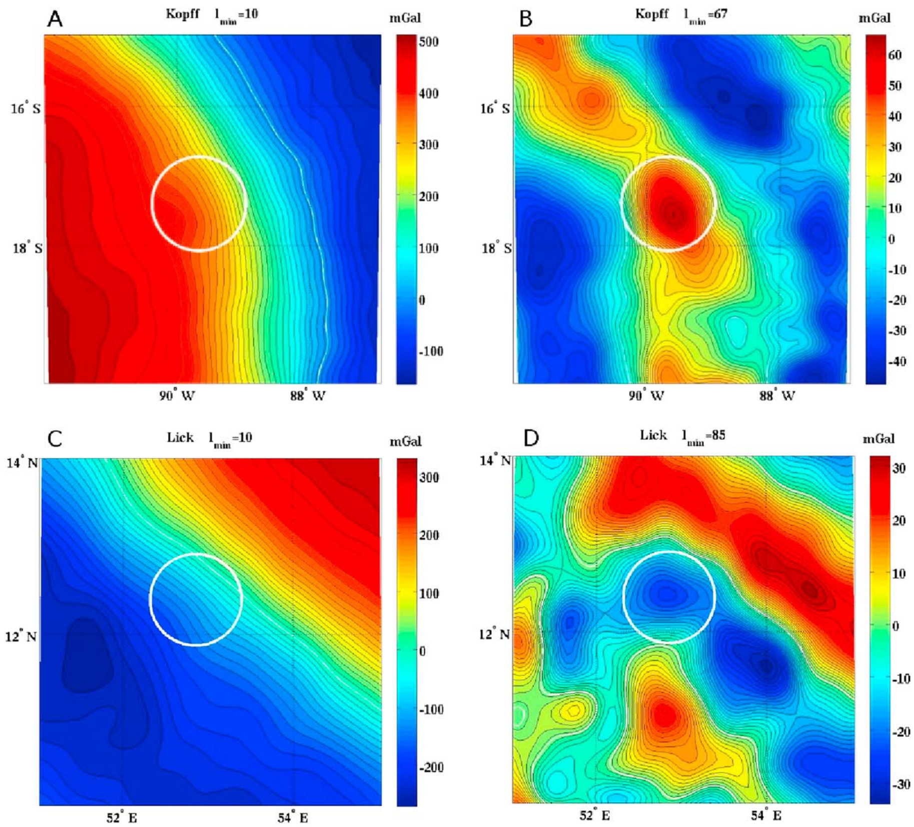

Figure 2. Comparison of the two methods of background removal with the craters (a, b) Kopff ($D = 31$ km) and (c, d) Lick ($D = 41$ km). Figures 2a and 2c use $l_{\mathrm{min}} = 10$, while Figures 2b and 2d use the spectral filtering technique (equation (3), $n = 4$). White circles indicate crater rims [*Head et al.*, 2010]. In the case of $l_{\mathrm{min}} = 10$ both craters have their signals overwhelmed by a strong long-wavelength regional signal (note the difference in scale). This signal is recovered by using the spectral filtering approach.

Here C and m are coefficients to be fit to the data, and ΔM is the mass anomaly derived from the Bouguer anomaly. In testing for this relationship we found the solution from the real and false craters were identical. The important difference between this and the linear $\bar{g}_B$ plots (see section 4) is that in testing for a power relationship, we lose information about the sign of the anomaly. Both the real and false craters show a trend of increasing Bouguer anomaly magnitude with diameter. This is likely due to the fact that the lunar Bouguer power spectrum is red, i.e., more power at longer wavelengths [*Zuber et al.*, 2013b]. Regardless of how the background signal is removed, there will be a larger, long-wavelength component in the g_B of larger craters creating this artificial trend. Because of this potential for fictitious results, we do not report any fits to equation (4).

3. Statistical Model

To determine how the crater Bouguer anomalies are affected by different parameters, we used a generalized linear model (GLM). This is an overdetermined system

$$\bar{\mathbf{g}}_{\mathbf{B}} = \mathbf{A}\mathbf{c}, \tag{5}$$

where the columns of the matrix **A** are the parameters being tested and **c** is the solved for column array containing the relationship between $\bar{g}_B$ and a given parameter (i.e., the slope). Table 1 gives a list of the different parameters that were tested. Interaction terms (e.g., $D\cdot\phi$) and squared terms (D^2) were also tested. Each model was evaluated using the Bayesian information criterion (BIC) [*Kass and Raftery*, 1995]. BIC values are ideal for comparing models with different numbers of parameters when there are a large number of observations. The model with the lowest BIC value is preferred.

The BIC value for each model was calculated as

$$\mathrm{BIC} = -2\cdot\ln\hat{L} + p\cdot\ln(N). \tag{6}$$

Table 1. Parameters Tested in the General Linear Model[a]

Parameter	Source
Diameter (*D*)	*Head et al.* [2010]
Crater age	*Losiak et al.* [2009]
Porosity (ϕ)[b]	*Wieczorek et al.* [2013] and *Besserer et al.* [2014]
Density gradient	*Besserer et al.* [2014]
Density *e*-folding depth	*Besserer et al.* [2014]
Grain density (ρ_g)	*Huang and Wieczorek* [2012]
Crustal thickness	*Wieczorek et al.* [2013]
Maria (logical)	*Nelson et al.* [2014]
SPA (logical)	*Head et al.* [2010]
g_B/D slope break[c]	*Soderblom et al.* [2015]

[a] Parameters labeled *logical* are entered into the matrix *A* as a set of 0 and 1 s (equation (5)).

[b] Porosity was calculated with the depth averaged density to 10 km for the *Besserer et al.* [2014] values.

[c] *Soderblom et al.* [2015] suggested that the g_B/D slope goes to 0 at $D = 93^{+47}_{-19}$ km. This is included in the matrix as an additional *D* dependence only applied to craters larger than the diameter break. This break in slope adds two free parameters (the change in slope and location of slope break), while all other parameters add one.

Here N is the number of observations, p is the number of model parameters, and $\ln \hat{L}$ is the model log likelihood. The model log likelihood was calculated as

$$\ln \hat{L} = \sum_{i=1}^{N} \ln \left(\frac{\exp(-E_i^2/2\sigma^2)}{\sqrt{2\pi\sigma^2}} \right). \tag{7}$$

Here E_i is the residual of each observation defined by

$$\mathbf{E} = \bar{\mathbf{g}}_\mathbf{B} - \mathbf{Ac}, \tag{8}$$

where σ is the standard deviation of **E**. Note that in order to meaningfully compare the BIC scores of two models, they must have the same number of observations.

Due to the large number of possible models, a stepping iterative approach was used. This operates by locally minimizing the BIC value by adding or removing parameters. This is a local minimization, so it is possible that there exists a better model in the parameter space. To try to mitigate this possibility, we ran this minimization multiple times starting with different starting parameters.

4. Results

4.1. Regional Differences

We find there are regional differences in the Bouguer anomaly of craters from the three lunar terranes (highlands, maria, and the South Pole-Aitken basin). These are most clearly expressed by statistically different $\bar{g}_B/D$ slopes as shown in Figure 3. The mean Bouguer anomaly of craters in each region is also statistically distinct. A similar plot can be constructed showing the $\bar{g}_B/\phi$ slopes in each region. Craters in each of the three lunar terranes have the same $\bar{g}_B/\phi$ relationship to within the 95% confidence intervals (see Figure 4). This is in part due to the fact that each of the three lunar terranes has a distinct porosity. The small range in porosity values leads to large uncertainty in these slope estimations. Because of this, it is more meaningful to compare the mean porosity in each terrane with the mean $\bar{g}_B$ (Figure 5). This figure shows that porosity is a strong control for the differences between the terranes, an observation that is more rigorously explored in the following sections.

4.2. Linear Model

The preferred GLM is

$$\bar{g}_B = D(c_1 + c_2\phi). \tag{9}$$

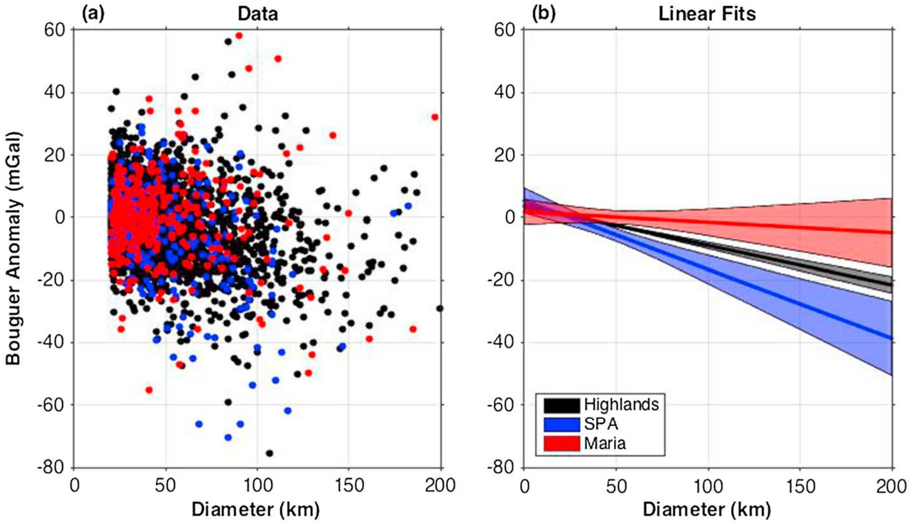

Figure 3. Crater g_b plotted against diameter. Both the (a) data and (b) best fit lines are shown for each of the three major lunar terranes. The black *highlands* crater group does not include craters in the SPA or Mare. Shaded regions are the 95% confidence intervals. The fact that the g_b/D slope varies in the three lunar terranes implies that slope is a function of ϕ (section 5).

In this equation ϕ is given as a percentage. This model is preferred over the next best model by a $\Delta\text{BIC} \approx 4$. $\Delta\text{BIC} = 4$ is interpreted as "strong evidence" for one model over the other [*Kass and Raftery*, 1995]. This model is preferred regardless of whether the constant *Wieczorek et al.* [2013] or linear *Besserer et al.* [2014] local density model is used. Bulk density can be substituted into equation (9) in place of porosity with no effect on the BIC score. This interchangeability is due to the fact that that g_B is uncorrelated with ρ_g. We choose to use porosity for ease of comparison with *Soderblom et al.* [2015] and *Milbury et al.* [2015].

We estimate values of $c_1 = -0.26 \pm 0.09$ mGal km^{-1} and $c_2 = 0.016 \pm 0.005$ mGal km^{-1} $\%_\phi^{-1}$. The values of c_1 and c_2 do vary slightly depending on the density model used and choices in crater filtering. To take this into account, we estimated c_1 and c_2 with each of the density models [*Wieczorek et al.*, 2013], linear [*Besserer et al.*, 2014] at 10 km and exponential [*Besserer et al.*, 2014] to 10 km. Estimates were also made rejecting craters with $\sigma_{\text{in}} > 20$ mGal. The values reported are the mean of these estimates, and the errors are the standard deviation of the different estimates (which is greater than the error of each individual estimate).

Adding a break in slope as was suggested by *Soderblom et al.* [2015] is not supported for any diameter in this range. When we exclude porosity from the regression we are able to find the same break in slope reported

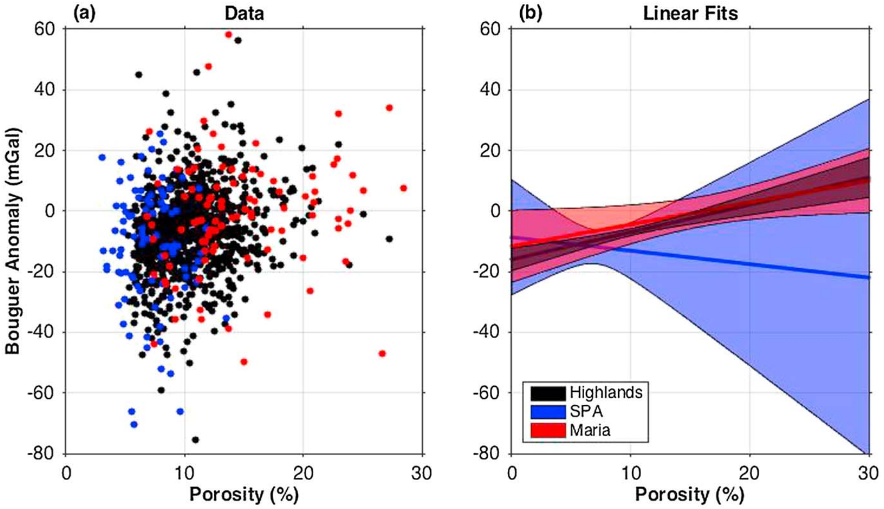

Figure 4. Same as Figure 3 only with porosity. All of the linear fits are identical to within their 95% confidence intervals.

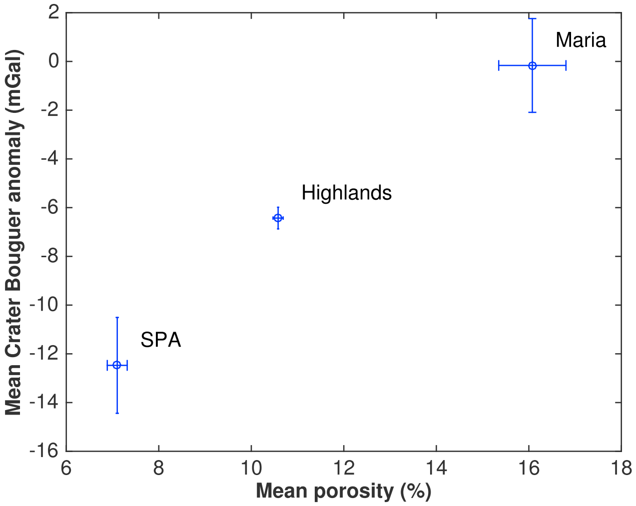

Figure 5. Mean crater Bouguer anomaly against mean porosity at each crater. Porosity was calculated using *Besserer et al.* [2014] linear model averaged to a depth of 10 km. Error bars show the standard error of each mean. The porosity of the maria should be viewed cautiously because the assumption of a linear density gradient [*Besserer et al.*, 2014] is likely not valid for the maria.

by *Soderblom et al.* [2015]. It is unclear if the break in slope is a spurious signal caused by reduced data density at larger diameters or if the signal is too weak for us to detect. Adding an additional term to accommodate a bulk offset or unique $\bar{g}_B/D$ slope (independent of ϕ) in each of these regions was also not preferred. This implies that the regional differences we see are explained by the interplay of D and ϕ in equation (9).

5. Discussion

Our best fit linear model, equation (9), captures the expected dependence of $\bar{g}_B$ on D and ϕ noted by *Soderblom et al.* [2015] and *Milbury et al.* [2015]. If the regional differences between the lunar highlands, SPA, and maria (Figure 3) were due to some parameter other than porosity, that would have entered the model as a third term. If porosity variations were not enough to explain the variations between the lunar terranes, the model would include a separate offset coefficient for the craters in SPA and the maria. Indeed this is what occurs if we remove porosity from the parameters to which the GLM has access.

A priori if we were to construct a linear dependence of $\bar{g}_B$ on D and ϕ, we might expect it to take the form

$$\bar{g}_B = c_1 D + c_2 \phi + c_3. \tag{10}$$

There are two separate reasons why equation (9) is not of this form. The first is that this intuitively simpler form (equation (10)) includes an additional parameter (c_3), which is necessary to attain an equivalent fit to the data but is penalized by the BIC criterion (equation (6)). The second reason is that we do need a term that depends on $D \cdot \phi$ to fully explain the regional differences observed. Figure 3 shows that $d\bar{g}_B/dD$ is different in each of the three lunar terranes. This implies, assuming ϕ is the controlling factor, that $d\bar{g}_B/dD$ is itself a function of ϕ. This is true in equation (9) but not in equation (10).

One way to interpret equation (9) is that it is showing the balance between two competing processes, both of which scale with diameter. The first, quantified by c_1, is the creation of new pore space by the impact [*Collins*, 2014]. The second, $c_2 \cdot \phi$, is the closure of preexisting pore space. This model suggests that for some particular initial porosity value, these two factors of opposite sign are approximately the same magnitude, resulting in $\bar{g}_B \sim 0$. This is consistent with the modeling work done by *Milbury et al.* [2015], who found that for an initial porosity of ~7%, $\bar{g}_B \sim 0$. The errorbars on our estimates of c_1 and c_2 are too large to make a meaningful estimate of this critical porosity value.

The above interpretation of equation (9) assumes that there are no other processes that scale with diameter aliasing into our model. This approach of correlating $\bar{g}_B$ with global lunar data sets is limited in the kinds of processes it can capture. In particular, the decrease in density a mineral can undergo due to the shock pressure of the initial impact may be comparable to those observed [*Ahrens et al.*, 1969; *Stoffler and Hornemann*, 1972; *Langenhorst and Deutsch*, 1994]. The shock pressures, however, drop off very quickly as you move away from the center of the crater [*Gault and Heitowit*, 1963; *Stoffler et al.*, 1975] which would strongly limit the volume of material affected. Still, it is possible that the amount of shocked minerals scales with the crater diameter which could in turn contribute to the values presented for c_1 and c_2. However, the data we have available do not allow us to quantify this.

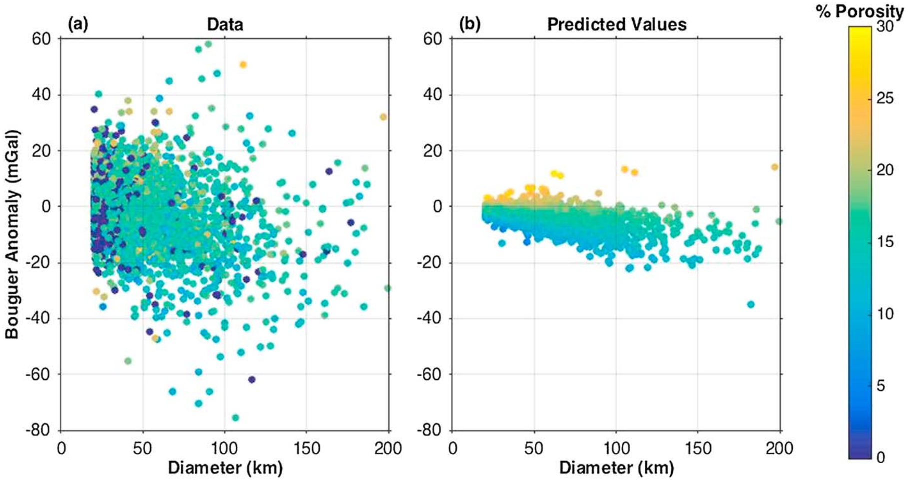

Figure 6. Plot of the (a) crater g_B versus D for the real craters and (b) what would be predicted by equation (9). While equation (9) captures the bulk trends there is still a lot of scatter in the data.

As noted in section 1.1, the porosity values for the lunar maria should be viewed with caution. *Wieczorek et al.* [2013] did not estimate for the density in the maria, and the linear density model model used by *Besserer et al.* [2014] is likely a poor approximation for the density structure in this region. Even ignoring the maria, our model implies that the reason craters in SPA have a distinct $\bar{g}_B$ signal is because of the low local porosity.

5.1. Sources of Scatter in Crater Bouguer Anomalies

Despite our efforts to include a wide range of possible predictors, we are still only explaining ~10% of the variance of $\bar{g}_B$ (R^2). This is visually shown in Figure 6 which compares the observed g_B to that predicted by equation (9). To understand this scatter it is important to consider the sources of g_B on the Moon. These sources can be characterized as the sum of contributions from mascon and peak-ring basins plus the contributions of porosity variations at a continuum of length scales (or wavelengths) [*Zuber et al.*, 2013b; *Wieczorek et al.*, 2013]. In addition to impact basins, at the largest scale, coherent distributions of porosity (hence g_B) are observed, for example, in SPA and in the farside highlands [*Zuber et al.*, 2013b; *Wieczorek et al.*, 2013; *Besserer et al.*, 2014]. We expect signals at this length scale to be removed from the data by our spectral filter (section 2.1).

At length scales of order D (≈100 km), the Bouguer anomalies of complex craters compete with the porosity structure to the extent that the level of detectability of these anomalies varies significantly from crater to crater. At intermediate length scales (order $5D$), the porosity distribution makes it difficult to obtain a consistent estimate of the background reference Bouguer anomaly from crater to crater. At both short and intermediate scales, porosity structures lead to considerable stochastic scatter in parametric plots (e.g., $\bar{g}_B$ versus D). Additionally, there is also a stochastic component of scatter due to factors such as variations in impact velocity, impact angle, impactor composition and strength, target fracture strength, and regional magmatic effects. That there is a large level of small wavelength variations in density is consistent with other analyses of the GRAIL data [*Jansen et al.*, 2014].

6. Conclusions

There are regional differences in the crater $\bar{g}_B$ for each of the three lunar terranes. A general linear regression suggests that g_B is a function of only D and ϕ as shown in equation (9). This is consistent with previous work by *Soderblom et al.* [2015] and *Milbury et al.* [2015]. This model can be used as a baseline for future studies looking to understand the $\bar{g}_B$ of lunar impact craters. Still, this model only explains ~10% of the variance in the lunar crater $\bar{g}_B$ signals. This implies that crater g_b is strongly controlled by the local impact environment and postimpact processes. Future models should look to understand this variation by looking at specific populations of craters [*Jozwiak et al.*, 2015].

Acknowledgments
Data used in this paper are archived on the NASA Planetary Data System Geosciences node. Crater information and crater $\bar{g}_B$ values are also provided in Table S1 in the supporting information. We would like to thank two anonymous reviews for their comments on this manuscript. Part of this work was supported by the GRAIL project and NASA grants NNX15AP90G and NNX12AL08G.

References

Ahrens, T. J., C. F. Petersen, and J. T. Rosenberg (1969), Shock compression of feldspars, *J. Geophys. Res.*, *74*(10), 2727–2746, doi:10.1029/JB074i010p02727.

Besserer, J., F. Nimmo, M. A. Wieczorek, R. C. Weber, W. S. Kiefer, P. J. McGovern, J. C. Andrews-Hanna, D. E. Smith, and M. T. Zuber (2014), GRAIL gravity constraints on the vertical and lateral density structure of the lunar crust, *Geophys. Res. Lett.*, *41*(16), 5771–5777, doi:10.1002/2014GL060240.

Collins, G. S. (2014), Numerical simulations of impact crater formation with dilatancy, *J. Geophys. Res. Planets*, *119*(12), 2600–2619, doi:10.1002/2014JE004708.

Dvorak, J., and R. Phillips (1977), The nature of the gravity anomalies associated with large young lunar craters, *Geophys. Res. Lett.*, *4*(9), 380–382, doi:10.1029/GL004i009p00380/full.

Gault, D. E., and E. D. Heitowit (1963), The partition of energy for hypervelocity impact craters formed in rock, in *Proceedings of the 6th Symposium on Hypervelocity Impact*, vol. 2, pp. 419–456, Natl. Aeronautics and Space Admin. Tech., Cleveland, Ohio.

Head, J. W., C. I. Fassett, S. J. Kadish, D. E. Smith, M. T. Zuber, G. a. Neumann, and E. Mazarico (2010), Global distribution of large lunar craters: Implications for resurfacing and impactor populations, *Science*, *329*(5998), 1504–1507, doi:10.1126/science.1195050.

Huang, Q., and M. A. Wieczorek (2012), Density and porosity of the lunar crust from gravity and topography, *J. Geophys. Res.*, *117*, E05003, doi:10.1029/2012JE004062.

Jansen, J. C., J. C. Andrews-Hanna, J. W. Head, Y. Li, W. S. Kiefer, J. M. Soderblom, G. J. Taylor, and M. T. Zuber (2014), Small scale density variations in the lunar crust as seen in GRAIL data, in *Proceedings of 45th Lunar and Planetary Science Conference*, vol. 45, pp. 2730, LPI Contribution No. 1777, Woodlands, Tex.

Jolliff, B. L., J. J. Gillis, L. A. Haskin, R. L. Korotev, and M. A. Wieczorek (2000), Major lunar crustal terranes: Surface expressions and crust-mantle origins, *J. Geophys. Res.*, *105*(1999), 4197–4216, doi:10.1029/1999JE001103.

Jozwiak, L. M., J. W. Head, and L. Wilson (2015), Lunar floor-fractured craters as magmatic intrusions: Geometry, modes of emplacement, associated tectonic and volcanic features, and implications for gravity anomalies, *Icarus*, *248*, 424–447, doi:10.1016/j.icarus.2014.10.052.

Kass, R. E., and A. E. Raftery (1995), Bayes factors, *J. Am. Water Resour. Assoc.*, *90*(430), 773–795.

Kiefer, W. S., R. J. Macke, D. T. Britt, A. J. Irving, and G. J. Consolmagno (2012), The density and porosity of lunar rocks, *Geophys. Res. Lett.*, *39*(7), L07201, doi:10.1029/2012GL051319.

Konopliv, A. S., et al. (2014), High-resolution lunar gravity fields from the GRAIL primary and extended missions, *Geophys. Res. Lett.*, *41*(5), 1452–1458, doi:10.1002/2013GL059066.

Langenhorst, F., and A. Deutsch (1994), Shock experiments on pre-heated α- and β-quartz: I. Optical and density data, *Earth Planet. Sci. Lett.*, *125*(1), 407–420.

Losiak, A., D. Wilhelms, C. Byrne, K. Thaisen, S. Weider, T. Kohout, K. O'Sullivan, and D. Kring (2009), A new lunar impact crater database, in *Proceeding of the 40th Lunar and Planetary Science Conference*, vol. 40, pp. 1532, LPI Contribution, Woodlands, Tex.

Milbury, C., et al. (2015), Pre-impact porosity controls the gravity signature of lunar craters, *Geophys. Res. Lett.*, *42*(17), 9711–9716, doi:10.1002/2015GL066198.

Nelson, D., S. Koeber, K. Daud, M. Robinson, T. Watters, M. Banks, and N. Williams (2014), Mapping lunar maria extents and lobate scarps using LROC image products, in *Proceedings of the 45th Lunar and Planetary Science Conference*, vol. 45, pp. 2861, LPI Contribution No. 1777, Woodlands, Tex.

Pilkington, M., and R. Grieve (1992), The geophysical signature of terrestrial impact craters, *Rev. Geophys.*, *92*, 161–181, doi:10.1029/92RG00192/full.

Smith, D. E. et al. (2010), Initial observations from the Lunar Orbiter Laser Altimeter (LOLA), *Geophys. Res. Lett.*, *37*(18), L18204, doi:10.1029/2010GL043751.

Soderblom, J. M., et al. (2015), The fractured Moon: Production and saturation of porosity in the lunar highlands from impact cratering, *Geophys. Res. Lett.*, *42*(17), 6939–6944, doi:10.1002/2015GL065022.

Stoffler, D., and U. Hornemann (1972), Quartz and feldspar glasses produced by natural and experimental shock, *Meteoritics*, *7*, 371–394.

Stoffler, D., D. E. Gault, J. Wedekind, and G. Polkowski (1975), Experimental hypervelocity impact into quartz sand: Distribution and shock metamorphism of Ejecta, *J. Geophys. Res.*, *80*(29), 4062–4077, doi:10.1029/JB080i029p04062.

Sugano, T., and K. Heki (2004), Isostasy of the Moon from high-resolution gravity and topography data: Implication for its thermal history, *Geophys. Res. Lett.*, *31*(24), L24703, doi:10.1029/2004GL022059.

Vaughan, W. M., and J. W. Head (2014), Impact melt differentiation in the South Pole-Aitken basin: Some observations and speculations, *Planet. Space Sci.*, *91*, 101–106, doi:10.1016/j.pss.2013.11.010.

Wieczorek, M. A., et al. (2006), The constitution and structure of the lunar interior, *Rev. Mineral. Geochem.*, *60*(1), 221–364.

Wieczorek, M. A., et al. (2013), The crust of the Moon as seen by GRAIL, *Science*, *339*(6120), 671–675, doi:10.1126/science.1231530.

Zuber, M. T., D. E. Smith, D. H. Lehman, T. L. Hoffman, S. W. Asmar, and M. M. Watkins (2013a), Gravity Recovery and Interior Laboratory (GRAIL): Mapping the lunar interior from crust to core, *Space Sci. Rev.*, *178*(1), 3–24.

Zuber, M. T., et al. (2013b), Gravity field of the Moon from the gravity recovery and interior laboratory (GRAIL) mission, *Science*, *339*(6120), 668–671, doi:10.1126/science.1231507.